Solid State Sciences 46 (2015) 102–106

Contents lists available at ScienceDirect

Solid State Sciences

journal homepage: www.elsevier.com/locate/ssscie

First-principles study on the electronic structures and magnetic properties of a diluted magnetic semiconductor $Ba_{1-x}K_x(Zn_{1-y}Mn_y)_2As_2$

J.T. Yang*, S.J. Luo*, Y.C. Xiong

School of Science, Hubei University of Automobile Technology (HUAT), Shiyan, Hubei, China

ARTICLE INFO

Article history:
Received 28 April 2015
Received in revised form
8 June 2015
Accepted 13 June 2015
Available online 17 June 2015

Keywords:
Decoupled charge and spin doping
Ferromagnetism
Electronic structure
First-principles calculations

ABSTRACT

Within Perdew-Burke-Ernzerhof generalized gradient approximation, first-principles calculations were performed to investigate the electronic structures and magnetic properties of II–II–V based DMS $(Ba,K)(Zn,Mn)_2As_2$ with holes doped via (Ba^{2+}, K^{1+}) replacements, and spins via isovalent (Zn^{2+}, Mn^{2+}) substitutions. Compound $BaZn_2As_2$ is paramagnetic semiconductor with a calculated band gap 0.28 eV. With Mn–Mn pair doped in different distances, $Ba(Zn_{1-y}Mn_y)_2As_2$ ($y = 0.03125$) system shows antiferromagnetic behaviour caused by the short-range superexchange interactions between localized spins of Mn^{2+} ions. Holes introduced by K dopants lead to metallic behaviour in $(Ba_{1-x}K_x)(Zn_{1-y}Mn_y)_2As_2$ system and drive the system toward ferromagnetism. The ferromagnetic coupling in the Mn–Mn pair is attributed to the long-range p–d exchange interactions mediated by itinerant holes. Competition between the antiferromagnetic superexchange and ferromagnetic interaction in the Mn–Mn pair determines the magnetic order of $(Ba_{1-x}K_x)(Zn_{1-y}Mn_y)_2As_2$ system, and the competition is dependent on both the concentration and distribution of K dopants.

1. Introduction

Diluted magnetic semiconductors (DMSs) have been widely investigated due to the possibility to utilize both charge and spin degrees of freedom [1–3]. As the prototype for III–V based DMSs, (Ga,Mn)As has been proposed as a promising for many spintronic device concepts [4–6]. However, the substitution of divalent (Ga^{3+}, Mn^{2+}) leads to the difficulty to individually control of the spin and charge degrees for (Ga,Mn)As. Moreover, metastable (Ga,Mn)As specimens are only available as thin films due to the limited chemical solubility of Mn in GaAs (<1%). Recently, some I–II–V based DMSs, such as Li(Zn,Mn)As and Li(Zn,Mn)P [7–9], are reported with decoupled hole and spin doping by controlling the contents of Li and Mn, respectively, and provide a way to overcome these difficulties. Shortly after the discovery of Li(Zn,Mn)As, some II-II-V based DMSs have been discovered, including $(Ba,K)(Zn,Mn)_2As_2$ [10], $(Ba,K)(Cd,Mn)_2As_2$ [11], and $(Sr,K)(Zn,Mn)_2As_2$ [12], via K dopant to introduce hole carriers and Mn dopant to supply magnetic moments. With successful 5~15% solid solutions Mn doping, the ferromagnetic temperature of $(Ba,K)(Zn,Mn)_2As_2$ bulks was reported up to 180 K.

As a new type of II-II-V based DMS, $(Ba,K)(Zn,Mn)_2As_2$ is an ideal prototype for theoretical study to elucidate the intrinsic physics of DMSs. Up to now, the theoretical data on the fundamental properties of $(Ba,K)(Zn,Mn)_2As_2$ is very limited. Used virtual crystal approximation (VCA) [13] to simulate the holes concentration, the ferromagnetism of $(Ba,K)(Zn,Mn)_2As_2$ is proposed as a variant of the classical double exchange by replacing the Hund's coupling by an effective p–d coupling [14]. However, the VCA can simulate the concentration of K dopants, but can't accurately simulate the influence of K concentration and distribution on the magnetic properties of $(Ba,K)(Zn,Mn)_2As_2$. Herein, to achieve the goal of understanding the magnetic mechanism of $(Ba,K)(Zn,Mn)_2As_2$, we carried out a first-principles study to get an insight into the electronic structures and magnetic properties of $(Ba,K)(Zn,Mn)_2As_2$ system with Mn–Mn pair and K dopants co-doped in different distributions, and investigated the influence of the dopants distribution on the magnetism.

* Corresponding authors.
E-mail addresses: jtyang@huat.edu.cn (J.T. Yang), sjluo@huat.edu.cn (S.J. Luo).

http://dx.doi.org/10.1016/j.solidstatesciences.2015.06.007
1293-2558/

2. Calculations methods

Based on the density functional theory (DFT), the Perdew-Burke-Ernzerhof generalized gradient approximation (PBE-GGA) was used in our calculations [15], implemented in the Vienna Ab-inito Simulation Package (VASP) [16] within the projector augmented wave (PAW) potential [17,18]. The plane waves cut-off energy of 400 eV, energy convergence of 10^{-5} eV and force convergence criterion of 10^{-3} eV/Å were used in present calculations. The Monkhorst-Pack grid was used for the unit cell $Ba(ZnAs)_2$ with $9 \times 9 \times 3$ k-points, and for the $4 \times 4 \times 1$ supercell $Ba(ZnAs)_2$ with $4 \times 4 \times 3$ k-points in the Brillouion zone including the Γ point centered. $Ba(ZnAs)_2$ crystallizes into a tetragonal $ThCr_2Si_2$-type structure with the space group I4/mmm, shown in Fig. 1(a). The optimized lattice constants of $a = b = 4.162$ Å and $c = 13.451$ Å are well consistent with the experimental value [19] of $a = b = 4.167$ Å and $c = 13.467$ Å, respectively. Since the PBE-GGA usually underestimates the band gap of semiconductors, a hybrid functional of HSE06 [20] approach was used to get the accurate electronic structure of pure $Ba(ZnAs)_2$ compound, implemented by VASP2-WANNIER90 code [21]. Using an 160-atom $4\times4\times1$ supercell ($Ba_{32}Zn_{64}As_{64}$), many $(Ba_{1-x}K_x)(Zn_{1-y}Mn_y)_2As_2$ systems were built via (Ba^{2+}, K^{+}) substitution and (Zn^{2+}, Mn^{2+}) substitution. Since holes introduced by K dopants leads to metallic behaviour in $Ba(ZnAs)_2$ [10], the electronic structures and magnetic properties of supercells $(Ba,K)(Zn,Mn)_2As_2$ are all achieved at the PBE-GGA level.

3. Results and discussions

3.1. Structures of $(Ba,K)(Zn,Mn)_2As_2$

Here, we investigate the electronic structure of pure compound $Ba(ZnAs)_2$. The band structures along some high symmetry points are depicted in Fig. 2, obtained by (a) PBE and (b) HSE06, respectively. Obviously, the PBE leads to be metallic-like behaviour in $Ba(ZnAs)_2$, while the HSE06 results in a nonmagnetic semiconductor of $Ba(ZnAs)_2$ with a narrow direct gap of 0.280 eV at the Γ point. The density of states (DOS) and projected DOS (PDOS) obtained by HSE06 are depicted in Fig. 2(d) and (c), respectively. The maximum of valence bands is dominantly composed of As 4p states and the minimum of conduction bands is primarily composed of Ba 5d states with a small amount of Zn 4s states. The valence bands between −4.0 and −0.5 eV are dominated by As 4p states, partly by Zn 4s and Ba 5d states. Between −6.5 and −4.0 eV, the Zn 4s orbitals hybrid closely with As 4p orbitals, forming a strong covalent Zn−As bond. In $Ba(ZnAs)_2$ unit cell, As atoms locate at the apexes of the Zn-centered tetrahedrons $[ZnAs_4]$, forming into quasi-two-dimensional blocks of $[ZnAs]_2$. The $[ZnAs]_2$ blocks and Ba layers are alternately stacked along the c axis. The charge transfer between the Ba layers and $[ZnAs]_2$ blocks was investigated by Bader analysis [22]. The excess charge on As atom and the depletion of electrons on each Zn atom and Ba atom were calculated to be 1.106e, -0.437e and −1.204e, respectively. The PDOS and Bader analysis reveal that the Zn−As bonds are mixed covalent-ionic, whereas the ionic bonds occur as $Ba^{\delta+}[ZnAs]_2^{\delta-}$ ($\delta \approx 1.21e$) between the $[ZnAs]_2$ blocks and Ba sheets. It can be seen that the charge reservoir Ba layer and the ferromagnetic $[ZnAs]_2$ blocks are spatially separated for $(Ba,K)(Zn,Mn)_2As_2$, and this structure is advantageous to control the amount of hole carriers and that of magnetic moments independently. Via off-stoichiometry of (Ba^{2+},K^{+}) substitutions, holes were introduced into $Ba^{\delta+}$ layer, and will affect the charge status of magnetic $[(Zn,Mn)As]_2^{\delta-}$ block, due to the strong interlayer ionic-type interaction. As a result, the magnetic behaviour of $[(Zn,Mn)As]_2^{\delta-}$ block can be transferred from antiferromagnetic (AFM) to ferromagnetic (FM).

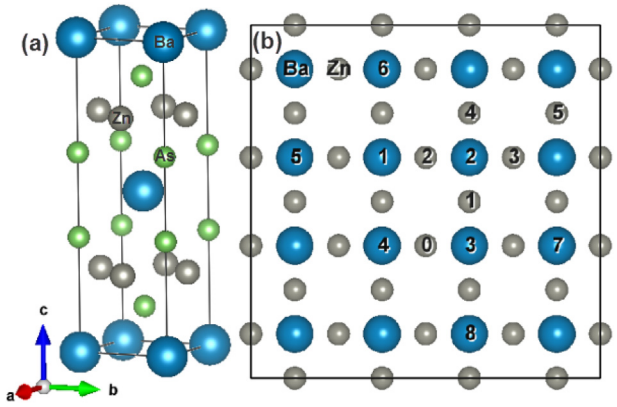

Fig. 1. (a) Schematic illustration of unit cell of $Ba(ZnAs)_2$. Blue, grey and green spheres represent Ba, Zn and As atoms, respectively. (b) A schematic view of two-dimensional Ba planes and Zn planes. The labels indicate the K doped and Mn doped sites, respectively. (For interpretation of the references to colour in this figure legend, the reader is referred to the web version of this article.)

3.2. Magnetic properties and electronic structures of $(Ba_{1-x}K_x)(Zn_{1-y}Mn_y)_2As_2$

Now, we study the effects of Mn and K co-doping to magnetic properties and electronic structures of $(Ba_{1-x}K_x)(Zn_{1-y}Mn_y)_2As_2$ ($y = 0.03125$) system with different K concentration ($x = 0.000$,0.0625 and 0.1250). The Mn−Mn pair substituted in the Zn layers is adopted to simulate the Mn doping for the case $y<<1$. Fig. 1(b) shows a schematic view of 2-dimensional Zn lattice (grey sphere) and the neighbouring Ba lattice (blue sphere). The number labels of the Zn lattice indicate the coplanar Mn−Mn pair configuration. One Mn atom is fixed at Zn site 0, another is placed at Zn sites 1–5. The Mn−Mn pair configuration is denoted as Mn@(0,n), and n from 1 to 5. The distances of different Mn−Mn pairs are presented in Tabel. 1. The nearest neighbour Mn−Mn configuration is named as Mn@(0,1), and the second nearest neighbour Mn−Mn configuration is named as Mn@(0,2), and so on. Similarly, the number labels of the Ba lattice indicate the K dopants distribution. For the K concentration of $x = 0.0625$, two K atoms substitute at Ba sites 2 and 4, respectively, named as K@(2,4). For $x = 0.125$, four K atoms substitute at Ba sites in three different K dopants distributions, named as K@(1–4), K@(2,4,6,8) and K@(1,3,5,7), respectively. Table 1 lists the calculated energies in FM alignment and AFM alignment, respectively, for $(Ba_{1-x}K_x)(Zn_{1-y}Mn_y)_2As_2$ systems with Mn@(0,n) and different K concentrations. The exchange energies, defined as $\Delta E = E(AFM)-E(FM)$, are plotted as a function of the distances of Mn−Mn pairs in Fig. 3. If $\Delta E > 0$, the ferromagnetism is more stable, or else the antiferromagnetism is more stable.

First, magnetic properties of $Ba_{32}Zn_{62}Mn_2As_{64}$ system with Mn@(0,n) were considered. The exchange energies were plotted as a function of distance of the Mn−Mn pair in 3, showing that the exchange energies of $Ba_{32}Zn_{62}Mn_2As_{64}$ with Mn−Mn pair dopant are negative, except for the Mn@(0,3), thus, the $Ba(Zn_{1-y}Mn_y)_2As_2$ system prefers AFM ground state without holes doping. The exchange energies curve of $Ba_{32}Zn_{62}Mn_2As_{64}$ decays strongly with the distance, indicating that the AFM coupling between the Mn−Mn pair is consistent with superexchange interactions [23]. Then, by introducing two K atoms to substitute two Ba atoms, supercells $Ba_{30}K_2Zn_{62}Mn_2As_{64}$ with Mn@(0,n)K@(2,4) were built, and the calculated exchange energies were depicted in Fig. 3. The results indicate that Potassium doping drives the $(Ba_{1-x}K_x)(Zn_{1-y}Mn_y)_2As_2$ system with Mn@(0,n)K@(2,4) ($n > 2$) toward ferromagnetism.

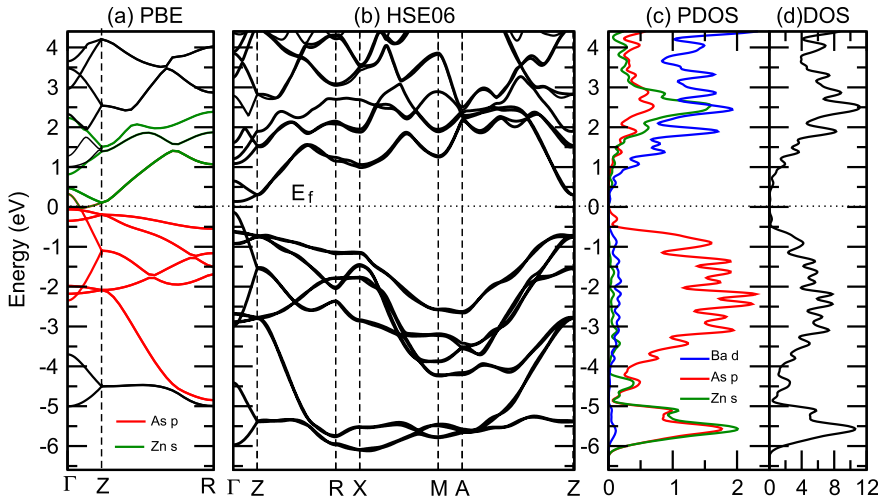

Fig. 2. The electronic structure of $Ba(ZnAs)_2$ obtained by (a) PBE and (b–d) HSE06. The high symmetry points are Γ(0.00 0.00 0.00), **Z** (0.00 0.00 0.50), **R** (0.00 0.00 0.50), **X** (0.50 0.00 0.00), **M** (0.50 0.50 0.00), and **A** (0.50 0.50 0.50), respectively, in the Brillouin zone.

Table 1
The distances (Å) of the different Mn–Mn pair, and the calculated energies (eV) of $Ba_{1-x}K_x(Cd_{1-y}Mn_y)_2As_2$ system in different Mn–Mn pair configuration with FM and AFM alignment with different K concentration *x*.

#	Distance	$x = 0.000$		$x = 0.1250$		$x = 0.0625$	
		E(*FM*)	*E*(*AFM*)	*E*(*FM*)	*E*(*AFM*)	*E*(*FM*)	*E*(*AFM*)
Mn@(0,1)	2.921	−558.8455	−559.1711	−544.6654	−544.9163	−539.8565	−539.9788
Mn@(0,2)	4.131	−558.9725	−559.1094	−544.7947	−544.8621	−539.9325	−539.9919
Mn@(0,3)	5.842	−559.0521	−559.0401	−544.8061	−544.8271	−539.9307	−539.9710
Mn@(0,4)	6.532	−559.0388	−559.0423	−544.8003	−544.8235	−539.9058	−539.9672
Mn@(0,5)	8.323	−559.0264	−559.0536	−544.8128	−544.8214	−539.8936	−539.9704

However, $Ba_{30}K_2Zn_{62}Mn_2As_{64}$ systems with Mn@(0,1)K@(2,4) and Mn@(0,2)K@(2,4) are AFM. Next, in order to improve the K concentration, we construct a supercell $Ba_{28}K_4Zn_{62}Mn_2As_{64}$ with K@(1–4) and Mn@(0,n), by locating four K atoms at Ba sites 1–4. It is found that the magnetic order of $(Ba_{1-x}K_x)(Zn_{1-y})Mn_y)$ system with Mn@(0,2) transfers from AFM to FM with the increasing of K concentration. Still, $(Ba_{1-x}K_x)(Zn_{1-y}Mn_y)_2As_2$ system with Mn@(0,1) remains AFM, caused by the strong AFM coupling of Mn moments in the nearest neighbour Mn–Mn pair. As a consequence, the FM coupling in the Mn–Mn pair is mediated by the holes introduced by K dopants. Moreover, since the K dopants are formed into a cluster, shown in Fig. 1(b), the FM interaction mediated by the holes is long-range. The FM behaviour of $(Ba_{1-x}K_x)(Zn_{1-y}Mn_y)_2As_2$ system results from the competition between the AFM superexchange and FM interaction mediated by holes introduced by K dopants. Due to the competition, the absolute exchange energy of AFM $(Ba_{1-x}K_x)(Zn_{1-y}Mn_y)_2As_2$ system with Mn@(0,1) is reduced about threefold, from |−325.59| meV ($x = 0.000$) to |−122.3| meV ($x = 0.125$).

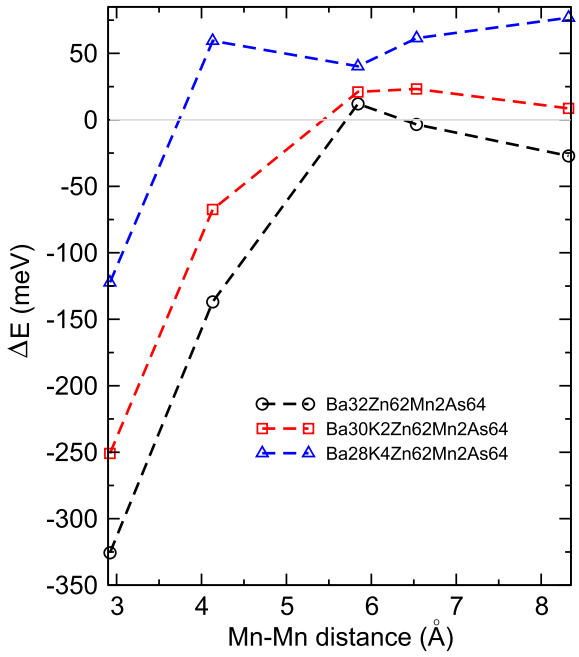

Fig. 3. The exchange energies Δ*E* (meV) as a function of distance (Å) of the Mn–Mn pair in supercells of $Ba_{32}Zn_{62}Mn_2As_{64}$, $Ba_{30}K_2Zn_{62}Mn_2As_{64}$ with K@(2,4) and $Ba_{28}K_4Zn_{62}Mn_2As_{64}$ with K@(1–4).

Further, we investigate the electronic structures of $(Ba_{1-x}K_x)(Zn_{1-y}Mn_y)_2As_2$ system, in order to clarify the magnetic coupling between the Mn–Mn pairs and itinerant holes. Since the magnetic behaviour is more multifarious, the electronic structures of $(Ba_{1-x}K_x)(Zn_{1-y}Mn_y)_2As_2$ system with Mn@(0,2) are discussed for simplicity. The total DOS and PDOS of (a) $Ba_{32}Zn_{62}Mn_2As_{64}$ with Mn@(0,2), (b) $Ba_{30}K_2Zn_{62}Mn_2As_{64}$ with Mn@(0,2)K@(2,4) and (c) $Ba_{28}K_4Zn_{62}Mn_2As_{64}$ with Mn@(0,2)K@(1–4) were calculated and plotted in Fig. 4. For comparison, the total DOSs of pure $Ba_{32}Zn_{624}As_{64}$ are plotted in Fig. 4. Shared as the same neighbour of the two Mn dopants, the PDOS of As2 atom is discussed and amplified 5 fold for clarity. Accordingly, the spin density distribution of $(Ba_{1-x}K_x)(Zn_{1-y}Mn_y)_2As_2$ system with Mn@(0,2) are illustrated in Fig. 5 by VESTA [24], as (a) for $Ba_{32}Zn_{62}Mn_2As_{64}$ with Mn@(0,2), (b) for $Ba_{30}K_2Zn_{62}Mn_2As_{64}$ with Mn@(0,2)K@(2,4)and (c) for

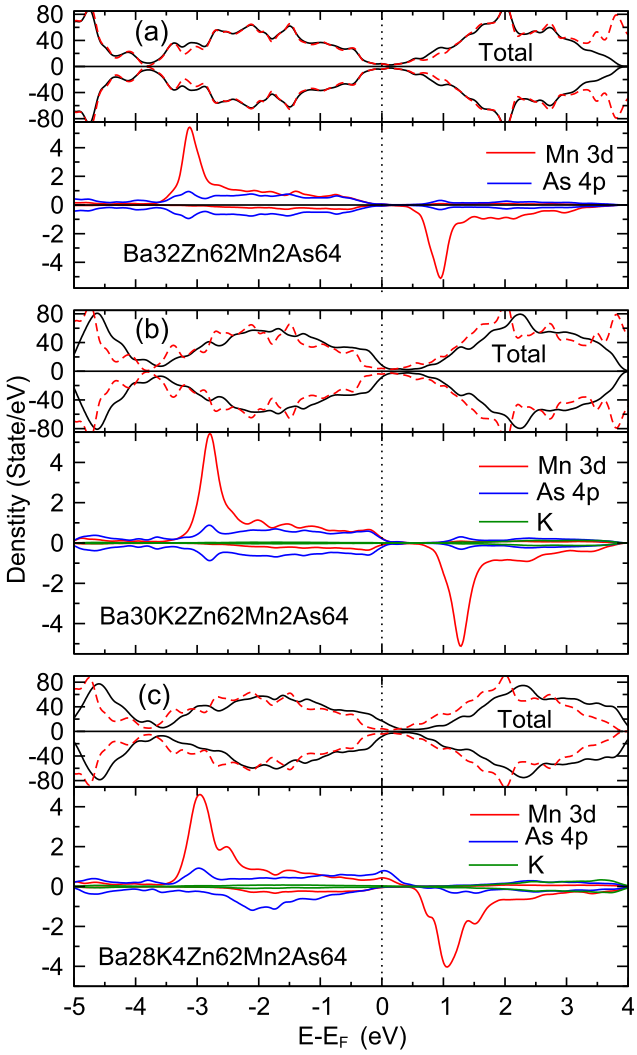

Fig. 4. The spin-polarized DOS and PDOS of (a) $Ba_{32}Zn_{62}Mn_2As_{64}$ with Mn@(0,2), (b) $Ba_{30}K_2Zn_{62}Mn_2As_{64}$ with Mn@(0,2)K@(2,4) and (c) $Ba_{28}K_4Zn_{62}Mn_2As_{64}$ with Mn@(0,2)K@(1–4), respectively. The PDOS of As_2 atom is amplified 5 fold. The red broken lines in the upper panels indicate the DOS of $Ba_{32}Zn_{64}As_{64}$. The Fermi level is denoted by the vertical dotted line at 0 eV. (For interpretation of the references to colour in this figure legend, the reader is referred to the web version of this article.)

$Ba_{28}K_4Zn_{62}Mn_2As_{64}$ with Mn@(0,2)K@(1–4). The spin density is defined as the difference in charge density between the spin up and spin down (i.e., $\Delta\rho = \rho_\uparrow - \rho_\downarrow$). The yellow and cyan isosurfaces represent positive and negative spin densities with value of $\pm 10^{-3}e/Å^3$, respectively.

The spin up DOS is identical to the spin down one for $Ba_{32}Zn_{62}Mn_2As_{64}$ with Mn@(0,2), consistent with its AFM ground state. Near the Fermi level, the DOSs of $Ba_{32}Zn_{62}Mn_2As_{64}$ with Mn@(0,2) coincides well with that of supercell $Ba_{32}Zn_{64}As_{64}$ (plotted by red broken lines), revealing that no holes was introduced into the supercell by Mn dopants. Shown in the lower panel of Fig. 4(a), the Mn 3d states demonstrate that ionic Mn is in high spin state and that Mn 3d orbitals strongly hybridize with the surrounding As 4p orbitals. The high spin state of ionic Mn is also confirmed in the spin density, showing that the spin densities mainly localize on Mn–Mn pair and partly on the surrounding As atoms. Although hybrid with the Mn 3d orbitals, there is no spin polarization in the spin-resolved PDOS of As2 atom which shared as the same neighbour of the two Mn dopants. Both the PDOS and the spin densities of $Ba_{32}Zn_{62}Mn_2As_{64}$ show that the AFM superexchange in the Mn–Mn pair is transferred by the As2 4p states. Shown in Fig. 4(b), the total DOS of $Ba_{30}K_2Zn_{62}Mn_2As_{64}$ with Mn@(0,2)K@(2,4) moves across the Fermi level, compared with that of $Ba_{32}Zn_{64}As_{64}$. Therefore, doping K atoms into Ba sites introduces holes, resulting in metallic behaviour in $Ba_{1-x}K_x(Zn_{1-y}Mn_y)_2As_2$. However, the spin up and spin down DOSs of $Ba_{30}K_2Zn_{62}Mn_2As_{64}$ with Mn@(0,2)K@(2,4) are still symmetrical, revealing its AFM ground state. As that of total DOS, the PDOS of $Ba_{30}K_2Zn_{62}Mn_2As_{64}$ also move toward the Fermi level. The K states hybrid with As 4p states in a wide energy region of the valence bands, revealing that the holes are delocalized and predominantly introduced into the top of valence bands composed mainly of As 4p states. With the AFM state, the spin densities of $Ba_{30}K_2Zn_{62}Mn_2As_{64}$ Mn@(0,2)K@(2,4) are similar as that of $Ba_{32}Zn_{62}Mn_2As_{64}$ Mn@(0,2), shown in 5 (b).

When the K concentration is increased, the total DOS of $Ba_{28}K_4Zn_{62}Mn_2As_{64}$ with Mn@(0,2)K@(1–4) pushes more states across the Fermi level, shown in Fig. 4(c), revealing that more holes are introduced into the system. Obtained by the Bader analysis, the number of valence electrons of As2 is 5.72*e* for $Ba_{28}K_4Zn_{62}Mn_2As_{64}$ with Mn@(0,2)K@(1–4), compared with 5.85*e* for $Ba_{30}K_2Zn_{62}Mn_2As_{64}$ with Mn@(0,2)K@(2,4), thus, the holes on As2 atom increase with the K concentration. The excess holes lead to the rise of long-range FM exchange interaction, which exceeds the short-range AFM superexchange interaction and results in the inverse transformation of AFM to FM for $Ba_{1-x}K_x(Zn_{1-y}Mn_y)_2As_2$ with Mn@(0,2). Shown in the PDOS, a significant spin polarization appears around the Fermi level. An exchange splitting between the spin up and spin down sates is also found around the Fermi level for As2 4p orbitals, indicating that the As2 plays an essential role in the magnetic interactions of $Ba_{1-x}K_x(Zn_{1-y}Mn_y)_2As_2$ with Mn@(0,2). For the As2 4p states of Mn@(0,2), the excess holes cause a strong repulsive interaction, which pushes the spin up states upward and cross the Fermi level, while the spin down states downward, leading to the evident spin-splitting. With the increasing of holes concentration, more peaks appear in the Mn 3d states, showing strong hybridization between As 4p states and Mn 3d states. As shown in Fig. 5(c), the magnetic coupling between As 4p states and Mn 3d states is AFM, accord with the localized magnetic moments 3.95 μ_B for Mn

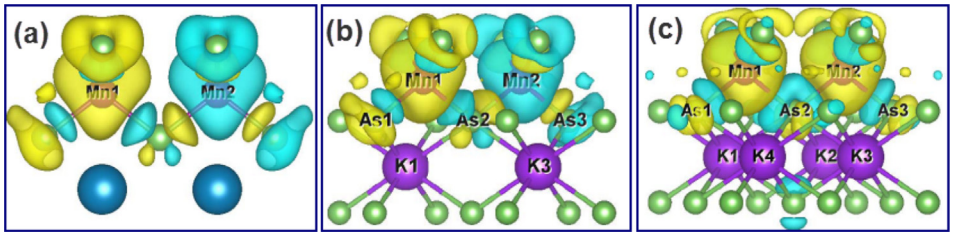

Fig. 5. Isosurface plot of the difference of spin up and spin down charges, $\Delta\rho=\rho_\uparrow-\rho_\downarrow$, as called the spin density. (a) $Ba_{32}Zn_{62}Mn_2As_{64}$ with Mn@(0,2), (b) $Ba_{30}K_2Zn_{62}Mn_2As_{64}$ with Mn@(0,2)K@(2,4) and (c) $Ba_{28}K_4Zn_{62}Mn_2As_{64}$ with Mn@(0,2)K@(1–4). Yellow and cyan isosurfaces represent positive and negative spin densities ($\pm 10^{-3}e/Å^3$), respectively. (For interpretation of the references to colour in this figure legend, the reader is referred to the web version of this article.)

and −0.05 μ_B for As2, respectively. The FM interactions in the Mn–Mn pair can be attribute to the p–d exchange interactions as $Mn_{\uparrow}$–$As_{\downarrow}$–$Mn_{\uparrow}$.

In order to investigate the influence of K dopants distribution on the magnetic properties of $Ba_{1-x}K_x(Zn_{1-y}Mn_y)_2As_2$ system, the magnetic ordering of $Ba_{28}K_4Zn_{62}Mn_2As_{64}$ with Mn@(0,n) K@(1,3,5,7) and Mn@(0,n)K@(2,4,6,8) was also considered. As discussed above, $Ba_{1-x}K_x(Zn_{1-y}Mn_y)_2As_2$ ($x = 0.0625$) system is FM in Mn@(0,n) ($n > 2$) configuration, and still AFM in Mn@(0,1) configuration. Particularly, $Ba_{28}K_4Zn_{62}Mn_2As_{64}$ is AFM ($\Delta E = -17.00$ meV) with Mn@(0,2)K@(1,3,5,7), whereas FM ($\Delta E = 28.28$ meV) with Mn@(0,2)K@(2,4,6,8). Doped with the same concentration of K dopants, the number of valence electrons is 5.83e for $Ba_{28}K_4Zn_{62}Mn_2As_{64}$ with Mn@(0,2)K@(1,3,5,7), almost equal to 5.84e for $Ba_{28}K_4Zn_{62}Mn_2As_{64}$ with Mn@(0,2)K@(2,4,6,8). The FM p–d exchange interactions determines the ferromagnetism for $Ba_{28}K_4Zn_{62}Mn_2As_{64}$ with Mn@(0,2)K@(2,4,6,8), where the four K dopants of K@(2,4,6,8) form into a chain parallels to the Mn–Mn pair of Mn@(0,2). Correspondingly, the K-chain of K@(1,3,5,7) is vertical to Mn@(0,2), and the AFM superexchange is dominant for $Ba_{28}K_4Zn_{62}Mn_2As_{64}$ with Mn@(0,2)K@(1,3,5,7). It confirms the competition of the short-range AFM superexchange and a long-range FM interaction between localized Mn spins. As that of dopants concentration, the distribution of K dopants also produce an effect on the magnetic properties of $Ba_{1-x}K_x(Zn_{1-y}Mn_y)_2As_2$ system.

4. Conclusions

In conclusion, we have performed a study of the electronic structure and magnetic properties of K and Mn co-doped $BaZn_2As_2$ using density functional theory within the generalized gradient approximation. $BaZn_2As_2$ is a paramagnetic semiconductor with a small gap of 0.28 eV obtained by a hybrid functional of HSE06. $Ba(Zn_{1-y}Mn_y)_2As_2$ system doped with Mn–Mn pair and without K atom is antiferromagnetism, caused by the superexchange interactions between localized spins of Mn^{2+} ions, except for the third nearest neighbour Mn–Mn pair configuration. Holes introduced by K dopants lead the magnetic state of $(Ba_{1-x}K_x)(Zn_{1-y}Mn_y)_2As_2$ system transfer from antiferromagnetism to ferromagnetism, except for the nearest neighbour Mn–Mn pair configuration. The ferromagnetism of $(Ba_{1-x}K_x)(Zn_{1-y}Mn_y)_2As_2$ system is caused by the long-range p–d exchange interactions interaction mediated by the itinerant holes, attribute to the as $Mn_{\uparrow}$–$As_{\downarrow}$–$Mn_{\uparrow}$. Competition between the antiferromagnetic superexchange and ferromagnetic interaction in the Mn–Mn pair determines the magnetic order of $(Ba_{1-x}K_x)(Zn_{1-y}Mn_y)_2As_2$ system. The magnetic competition is dependent on both the concentration and distribution of K dopants.

Acknowledgements

This work is supported by Science Foundation for the young scholars of Hubei University of Automotive Technology (HUAT, No. 2012XQ08) and Major Scientific Research Project Pre-funds of HUAT (No. 2014XY06).

References

[1] T. Dietl, H. Ohno, Rev. Mod. Phys. 86 (2014) 187.
[2] T. Dietl, Nat. Mater. 9 (2010) 965.
[3] T. Jungwirth, Jairo Sinova, J. Mašek, J. Kucera, A.H. MacDonald 78 (2006) 809.
[4] H. Ohno, A. Shen, F. Matsukura, A. Oiwa, A. Endo, S. Katsumoto, Y. Iye, Appl. Phys. Lett. 69 (1996) 363.
[5] X.Z. Yu, H.L. Wang, D. Pan, et al., Nano. Lett. 13 (2013) 1572.
[6] H. Katayama-Yoshida, K. Sato, T. Fukushima, M. Toyoda, H. Kizaki, V.A. Dinh, P.H. Dederichs, Phys. Stat. Sol.(a) 204 (2007) 15.
[7] J. Mašek, J. Kudrnovská, F. Máca, B.L. Gallagher, R.P. Campion, D.H. Gregory, T. Jungwirth, Phys. Rev. Lett. 98 (2007) 067202.
[8] Z. Deng, K. Zhao, B. Gu, W. Han, J.L. Zhu, X.C. Wang, X. Li, Q.Q. Liu, R.C. Yu, T. Goko, B. Frandsen, L. Liu, J.S. Zhang, Y.Y. Wang, F.L. Ning, S. Maekawa, Y.J. Uemura, C.Q. Jin, Phys. Rev. B 88 (2013) 081203(R).
[9] Z. Deng, C.Q. Jin, Q.Q. Liu, X.C. Wang, J.L. Zhu, S.M. Feng, L.C. Chen, R.C. Yu, C. Arguello, T. Goko, F. Ning, J. Zhang, Y. Wang, A.A. Aczel, T. Munsie, T.J. Williams, G. M.Luke, T. Kakeshita, S. Uchida, W. Higemoto, T.U. Ito, Bo Gu, S. Maekawa, G.D. Morris, Y.J. Uemura, Nat. Commun. 2 (2011) 422.
[10] K. Zhao, Z. Deng, X.C. Wang, W. Han, J.L. Zhu, X. Li, Q.Q. Liu, R.C. Yu, T. Goko, B. Frandsen, L. Liu, F. Ning, Y.J. Uemura, H. Dabkowska, G.M. Luke, H. Luetkens, E. Morenzoni, S.R. Dunsiger, A. Senyshyn, P. Böni, C.Q. Jin, Nat. Commun. 4 (2013) 1442.
[11] X. Yang, Y. Li, P. Zhang, H. Jiang, et al., J. Appl. Phys. 114 (2013) 223905.
[12] X. Yang, Qi Chen, Y. Li, Z. Wang, J. Bao, Y. Li, Q. Tao, G. Cao, Z. Xu, EPL 107 (2014) 67007.
[13] J.K. Glasbrenner, J.P. Velev, I.I. Mazin, Phys. Rev. B 89 (2014) 064509.
[14] J.K. Glasbrenner, I. Zutić, I.I. Mazin, Phys. Rev. B 90 (2014), 140403(R).
[15] J.P. Perdew, K. Burke, M. Ernzerhof, Phys. Rev. Lett. 77 (1996) 3865.
[16] G. Kresse, J. Hafner, Phys. Rev. B 47 (1993) R558, 49 (1994) 14251; G. Kresse and J. Fürthmüller, Comput, Mater. Sci. 6 (1996) 15.
[17] P.E. Blöchl, Phys. Rev. B 50 (1994) 17953.
[18] G. Kresse, D. Joubert, Phys. Rev. B 59 (1999) 1758.
[19] A. Hellmann, A. Loehken, A. Wurth, Z. Mewis, Naturforsch. B 62 (2007) 155.
[20] A.V. Krukau, O.A. Vydrov, A.F. Izmaylov, G.E. Scuseria, J. Chem. Phys. 125 (2006) 224106.
[21] A.A. Mostofi, J.R. Yates, Y.S. Lee, I. Souza, D. Vanderbilt, N. Marzari, Comput. Phys. Commun. 178 (2008) 685.
[22] W. Tang, E. Sanville, G. Henkelman, J. Phys. Condens. Matter 21 (2009) 084204.
[23] J.N. Lalena, D.A. Cleary, Principles of Inorganic Materials Design, second ed., John Wiley and Sons, New York, 2010, pp. 345–346.
[24] K. Momma, F. Izumi, J. Appl. Crystallogr. 44 (2011) 127.